

On-chip photothermal gas sensor based on a lithium niobate rib waveguide

Yue Yan,[1,#] Hanke Feng,[2,#] Cheng Wang,[2,*] Wei Ren[1,*]

[1]Department of Mechanical and Automation Engineering, and Shenzhen Research Institute, The Chinese University of Hong Kong, New Territories, Hong Kong SAR, China
[2]Department of Electrical Engineering & State Key Laboratory of Terahertz and Millimeter Waves, City University of Hong Kong, Kowloon, Hong Kong SAR, China
[#]These authors contributed equally.
[*]Corresponding authors: cwang257@cityu.edu.hk, renwei@mae.cuhk.edu.hk

Abstract

On-chip optical gas sensors have attracted a lot of attention in many fields such as the internet of things and point-of-care diagnosis due to their compactness and high scalability. However, the current laser-based on-chip absorption gas sensors have limited sensitivity caused by the optical thin property and strong interference fringe noise. Here, we report sensitive on-chip photothermal gas detection on an integrated lithium niobate photonic platform. The evanescent wave of the frequency-modulated pump light (2004 nm) on a nanophotonic lithium niobate rib waveguide (length of 91.2 mm) is absorbed by the target gas molecules (carbon dioxide, CO_2), leading to the significant refractive index modulation of the rib waveguide due to the photothermal effect. A probe light (1550 nm) transmitted through the same waveguide undergoes the photothermal-induced phase modulation, which is sensitively detected by a heterodyne interferometer. As a proof of concept, we demonstrate the on-chip photothermal detection of CO_2 with a minimum detection limit of 1.2×10^{-4} cm^{-1}. This work provides new insight for future on-chip gas sensor development with high sensitivity and robustness.

Keywords: On-chip; photothermal spectroscopy; gas detection; lithium niobate; waveguide

1. Introduction

On-chip gas sensing has attracted significant attention due to its small size, low cost, and prospects for high-density integration, with potential applications ranging from environmental monitoring to biomedical diagnosis [1, 2]. By integrating the internet of things (IoT) technology, on-chip gas sensors are promising for building large sensing networks for distributed monitoring applications. In biomedical diagnosis, compact on-chip gas sensors are important for point-of-care diagnostic tools like portable breath analyzers [3]. Moreover, with the increasingly mature technologies of integrated photonics and foundry services, it is possible to develop highly scalable on-chip sensing systems densely integrated with gas sensors and a full range of functional photonic elements such as interferometers and modulators [4-6].

One common method for developing an on-chip gas sensor is to utilize the interaction between the evanescent field and the analyte [7, 8]. Evanescent-wave on-chip gas sensors have demonstrated a detection limit down to parts-per-million (ppm) level on a silicon waveguide [9]. Migrating the laser absorption sensor to an integrated photonic platform enables a monolithic sensing chip with substantial cost-benefit and scalability [10, 11]. However, the detection sensitivity of on-chip absorption gas sensors is constrained by the limited light-gas interaction length. The interaction length could be improved by leveraging the slow light effect, but the performance of these photonic devices is still limited by their large propagation loss [12, 13]. Some other spectroscopic methods such as wavelength modulation spectroscopy (WMS) and mid-infrared absorption spectroscopy have been adopted to improve the sensor performance [14-17]. In general, current evanescent-wave-based on-chip gas sensors encounter serious interference fringe noise induced by the waveguide facet reflection and roughness [18], which is hardly avoided in absorption spectroscopy.

Instead of directly measuring light intensity attenuation, photothermal spectroscopy (PTS) is an emerging method with high sensitivity by probing the photothermal-induced phase change via interferometry [19-21]. Recently, by taking advantage of the stronger optical field confinement to enhance the photothermal effect, PTS in a hollow-core fiber (HCF) enables sensitive gas detection with extremely high sensitivity and dynamic range [22-24]. In a typical PTS system with a pump-probe configuration, gas absorption of the modulated pump light dissipates heat to the surrounding which subsequently modulates the refractive index (RI) of the gas medium. The RI variation modulates the phase of a following probe laser that propagates through the same path as the pump laser in the gas medium. Only the photothermal-induced phase modulation signal can be picked up by the heterodyne interferometer, which effectively eliminates the background interference fringe noise. Additionally, compared to HCFs with a core diameter of tens of micrometers, realizing PTS in a sub-micrometer integrated photonic waveguide typically further enhances the photothermal effect. Hence, it usually increases the detection signal-to-noise ratio (SNR) by performing PTS in a photonic device such as the nanophotonic lithium niobate waveguide.

Nanophotonic lithium niobate ($LiNbO_3$, LN) is an ideal platform for high-sensitivity on-chip PTS considering its wide transparent window (350 nm – 5 μm), low optical loss, high thermo-optic coefficient and good scalability [25, 26]. More importantly, it is endowed with a variety of functional nanophotonic devices such as high-quality-factor micro-resonators, high-bandwidth and low-power optical modulators, broadband frequency-comb sources, and on-chip spectrometers [27-31]. The prospect of integrating multi-functional chip-scale devices on a single nanophotonic LN-on-insulator chip potentially enables a compact sensing platform for smart, low cost and highly scalable sensing applications.

Here, we report photothermal gas sensing on a nanophotonic LN platform for the first time. Using a 91.2 mm low-loss rib waveguide fabricated on an LN thin film, we demonstrate the detection of carbon dioxide (CO_2) at 4989.97 cm^{-1} (2004 nm) as a proof of concept. This novel on-chip photothermal gas sensor achieves a detection limit of 1.2×10^{-4} cm^{-1}, which is much more sensitive and robust compared to the direct absorption measurement.

2. Fundamentals of on-chip photothermal spectroscopy

Gas absorption of the pump laser in the air-cladding dissipates the localized heat to the solid waveguide, which causes the temperature variation of the waveguide. Fig. 1(a) shows the fabricated meandering LN waveguide with a total physical length of 91.2 mm; an SEM image of the LN waveguide is illustrated in Fig. 1(b). The LN waveguide dimensions are chosen to balance the evanescent field factor and optical loss (see more details on the model and fabrication process in Methods). Fig. 1(c) depicts the basic physical processes involved in the proposed on-chip photothermal gas sensing. Unlike the conventional photothermal detection in an HCF or free space, on-chip photothermal detection mainly utilizes the RI change in a solid waveguide instead of gas. The photothermal-induced RI change causes the phase shift of the probe laser propagating in the waveguide. Since the thermo-optic coefficient of air (-0.91×10^{-6}/K [32]) is much smaller than that of LN (extraordinary direction: 32.4×10^{-6}/K [33]), the on-chip phase modulation can be substantially enhanced compared to that achieved in the gas medium.

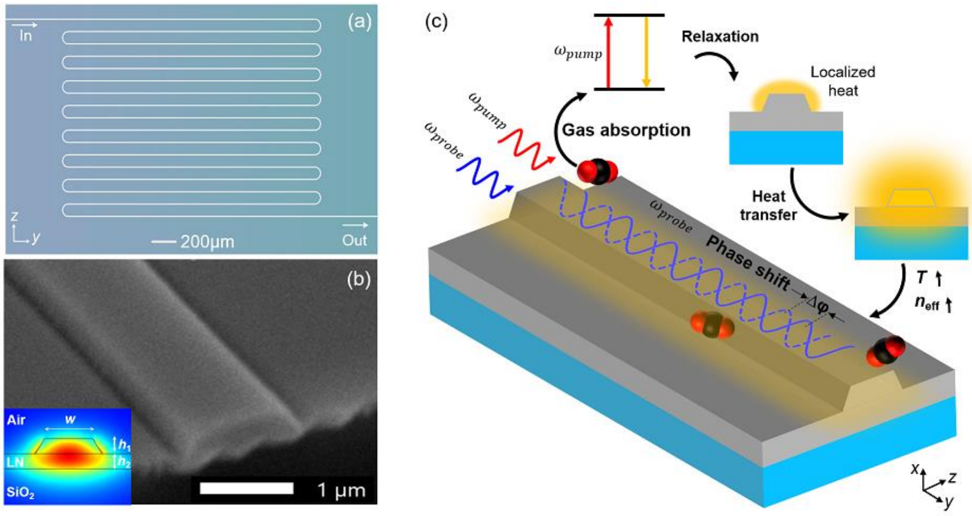

Fig. 1. (a) False-color wide-field microscope image of the LN waveguide. (b) SEM image of the LN waveguide. Inset: LN waveguide model and electric field profile of the TE_0 mode at 2004 nm. The LN film is not fully etched to the substrate, leaving $h_1 = h_2 = 250$ nm and $w = 800$ nm. (c) Principle of on-chip photothermal gas sensing.

Fig. 2(a) depicts the simulated heat source distribution originated from CO_2 absorption with an absorption coefficient of 0.12 cm^{-1} at the pump wavelength of 2004 nm and optical power of 1 mW. The on-chip photothermal dynamics are described in Methods and the simulation details are provided in Supplementary Note 1. The peak heat density reaches as high as 8.7×10^9 W/m^3 due to the strong optical confinement of the guided TE_0 mode. The heat source is sinusoidally modulated at the modulation frequency of the pump laser. At the center of the LN waveguide, Fig. 2(b) shows the time-dependent photothermal modulation dynamics with the pump laser frequency modulated at 5 kHz. The temperature of the LN waveguide increases from the initial 295 K because of the heat conduction from the air-cladding to the waveguide. The temperature variation ΔT reaches a plateau level after 100 ms, indicating the steady state of heat conduction. Besides the overall trend of temperature increase, a periodic variation of temperature with a small amplitude of 0.83 mK is observed as shown in the inset graph of Fig. 2(b). This periodic temperature variation induces an RI modulation to be detected by the probe laser beam. Due to the birefringence of the LN crystal [33], it has the largest positive thermo-optical coefficient along the z-direction, which aligns with the major electric field component of the TE_0 mode in this study. Fig. 2(c) presents the temperature distribution when the waveguide reaches equilibrium at 100 ms. The effective RI modulation of the TE_0 mode for the probe laser at 1550 nm is estimated to be 2.7×10^{-8}, corresponding to 10 mrad phase modulation for the 91.2 mm waveguide.

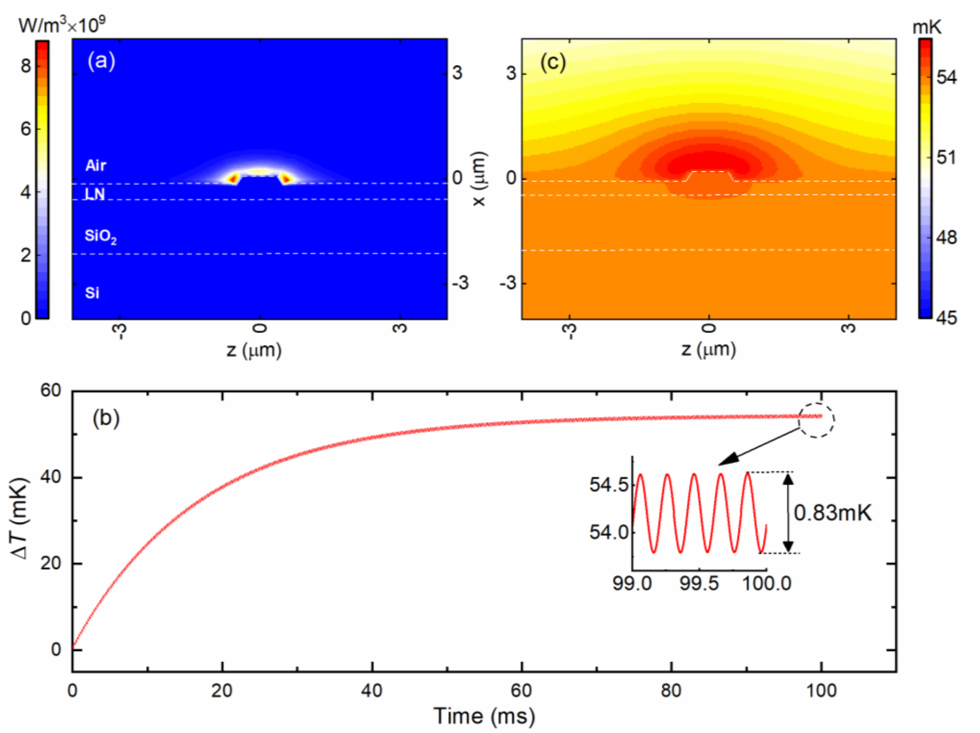

Fig. 2. (a) Simulated heat source distribution in the LN waveguide caused by CO_2 absorption of a 1-mW pump laser at 2004 nm. The heat source is sinusoidally modulated as $Q' = Q(1+sin(2\pi ft))/2$, where f is the modulation frequency of the pump laser. (b) Time-dependent temperature variation of the LN waveguide. Inset: the magnified region between 99-100 ms. (c) Temperature distribution at 100 ms of the heat transfer process.

3. Experimental setup

Fig. 3 depicts the schematic of the on-chip photothermal heterodyne gas sensing experiment. A distributed feedback diode laser is sinusoidally modulated at 5 kHz and its wavelength is slowly triangle-scanned at 250 mHz to cover the R(16) absorption line of CO_2 at 2004 nm. A probe laser at 1550 nm is used as the light source in the heterodyne interferometer. The pump and probe beams are coupled with a wavelength division multiplexer (WDM) and launched into the waveguide via a lensed fiber. The LN rib waveguide is placed in the sensing arm, whereas the reference arm is frequency-shifted by 70 MHz using an acousto-optic modulator (AOM). The heterodyne output (PD1) generates a beat note signal at 70 MHz and is further demodulated by a lock-in amplifier. More details of the heterodyne detection are provided in Methods. The LN chip is fixed on a brass holder with the temperature actively controlled (stability ±10 mK) by a thermoelectric cooler (TEC). The entire experimental setup is enclosed in a sealed chamber to be filled with the target gas mixtures. A free-space path of 120 mm is used as a reference measurement inside the same chamber.

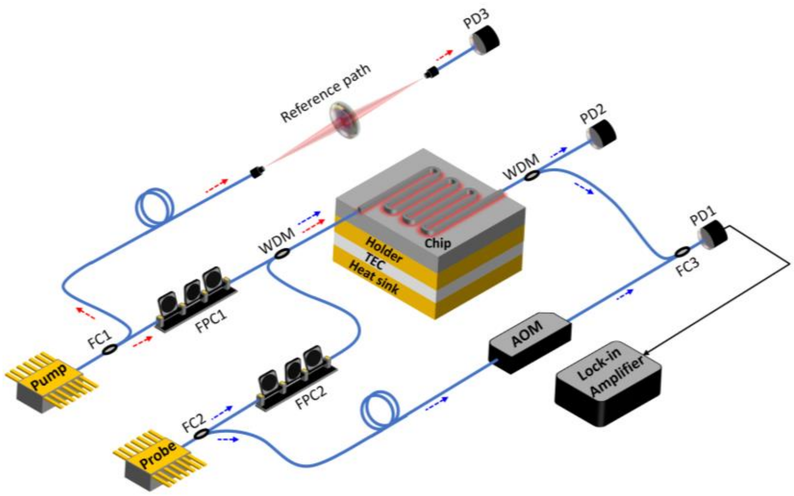

Fig. 3. Experimental setup of on-chip photothermal spectroscopy with heterodyne detection. Two lensed fibers (focal spot ~3 μm) are used to couple the laser in and out of the LN waveguide. Two fiber polarization controllers (FPCs) are used for the pump and probe beams to achieve the TE_0 mode propagation in the LN waveguide. FC: fiber coupler (splitting ratio 90/10); WDM: wavelength division multiplexing; AOM: acousto-optic modulator; PD: photodetector.

4. Results and discussion

We show the drastically improved SNR of gas on-chip detection using the proposed PTS approach compared to the traditional absorption spectroscopy. The transmitted signal (PD2) of edge-coupled integrated photonic waveguides commonly sees substantial interference fringes due to light reflections between the two waveguide facets. As shown in Fig. 4 (a), with pure nitrogen filled in the gas chamber, the fringe pattern varies significantly even at a small temperature change of 2˚C. By modulating the pump laser at 5 kHz, Fig. 4(b) shows the demodulated 2[nd]-harmonic signals of wavelength modulation spectroscopy (WMS-2*f*) of 54% CO_2 at two different chip temperatures. The WMS-2*f* signals are significantly distorted by the fringe noise. In contrast, the heterodyne photothermal 2[nd]-harmonic (PTS-2*f*) measurement shows much improved SNR under the same experimental condition, as shown in Fig. 4(c). By evaluating the peak amplitude and 1σ value of the PTS-2*f* signal with the pump laser off, we obtain a SNR of 60 for the measurement of 54% CO_2.

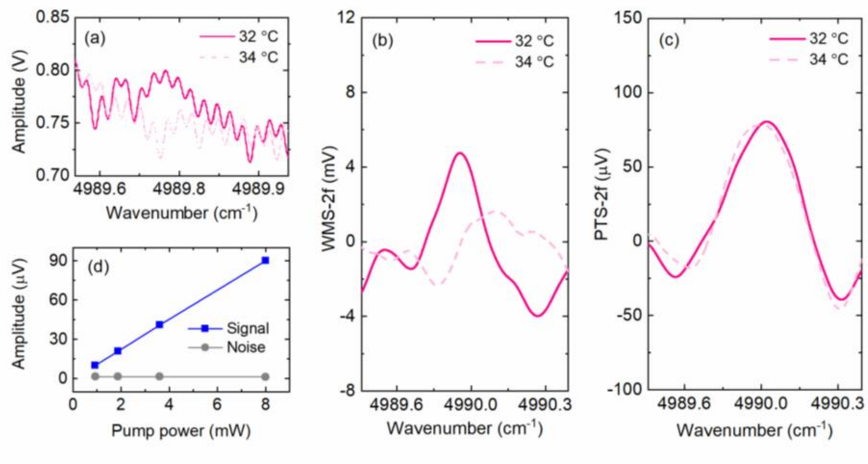

Fig. 4. (a) Measured transmission signal (pure N_2) of the pump light through the LN waveguide at 32℃ and 34℃, respectively. (b) Absorption signal (WMS-2*f*) of 54% CO_2. The signal can hardly be differentiated due to the large fringe noise. (c) Photothermal signal (PTS-2*f*) of 54% CO_2. (d) Variation of the PTS-2*f* amplitude with the pump power level. The noise remains almost unchanged at different power levels.

The laser parameters such as modulation frequency and amplitude are optimized to be 5 kHz and 140 mV, respectively, to achieve the best SNR of PTS-2*f* measurement; more details are provided in Supplementary Note 2. As the heat dissipation is proportional to the pump intensity, we further demonstrate the measurements of 54% CO_2 at different power levels of the pump laser. Fig. 4(d) presents the excellent linearity between the input pump power and PTS-2*f* amplitude, while the noise remains almost unchanged. It is worth noting that the pump power in the LN waveguide is much less than the input laser power due to the large loss of facet coupling (5.9 dB); more details of the propagation loss estimation are provided in Methods.

Although the on-chip photothermal signal is hardly affected by the fringe noise, we should not ignore the intrinsic material absorption by the LN waveguide. Fortunately, the material absorption is stable and can be subtracted as background from the measurement (Supplementary Note 3). Fig. 5(a) shows the linear response of the PTS-2*f* amplitude to CO_2 concentration between 6.8 % and 54%. Based on the input pump power (8 mW), 1σ noise level (1.33μV), and detection bandwidth (1.44 Hz), we estimate a normalized noise equivalent absorption coefficient (NNEA) of 9.3×10^{-6} $cm^{-1}\cdot W\cdot Hz^{-1/2}$. Allan deviation analysis is also conducted to evaluate the long-term stability of the on-chip photothermal system. As shown in Fig. 5(b), the PTS system achieves a detection limit of 870 ppm at the integration time of 190 s, corresponding to an absorption coefficient of 1.2×10^{-4} cm^{-1}.

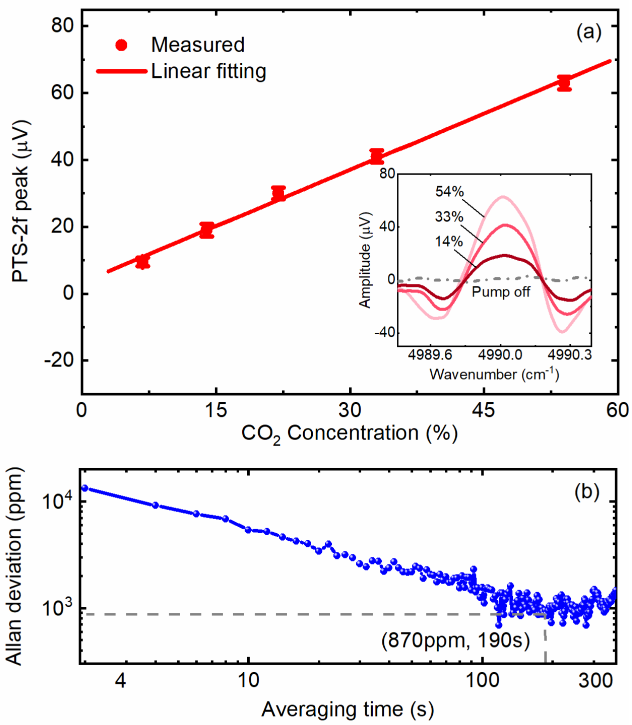

Fig. 5. (a) Variation of the PTS-2*f* peak amplitude with CO_2 concentration. Inset: representative PTS-2*f* spectra measured under different CO_2 concentrations. (b) Allan deviation (ppm) analysis of the on-chip PTS sensor.

Such an on-chip PTS scheme may achieve even higher SNR for trace gas sensing. Firstly, the high-power pump lasers could be implemented for higher sensitivity as the PTS signal increases linearly with the pump power. The on-chip optical power could be substantially increased by reducing the coupling loss using a high-NA free-space focusing lens or adiabatic mode spot-size converter [34]. Secondly, a higher evanescent field factor in the air-cladding could be designed to enhance the light-matter interaction. The current waveguide features an evanescent field factor of 6.9% in the air-cladding (Supplementary Note 4), which could be increased to 16% by designing a suspended waveguide structure (Supplementary Note 1). It also helps maintain the absorption-induced heat production within the suspended structure to improve the sensitivity (Supplementary Note 1). Note that a larger evanescent field may introduce a larger propagation loss, which should be evaluated systematically in the sensor design. Additionally, the environmental disturbance would introduce polarization noise in the fiber-optic interferometry. This problem could be mitigated by using polarization maintenance fibers or implementing on-chip interferometry.

5. Conclusion

In summary, we report for the first time on-chip photothermal spectroscopy for sensitive gas detection on a nanophotonic LN platform. Compared to on-chip absorption spectroscopy, our method shows dramatically improved SNR due to the significantly reduced fringe noise. With a 91.2 mm long LN rib waveguide, we achieve a detection limit of 870 ppm CO_2 at 190 s integration time, and demonstrate the sensor robustness under the disturbance of chip temperature. Different from on-chip absorption spectroscopy which is limited by the absorption path length, on-chip PTS could potentially overcome this limitation by using more sensitive phase detection methods. For instance, a micro-resonator-based interferometer can be monolithically integrated in a single chip for higher sensitivity [35]. More importantly, LN integrated photonics platform could support on-chip interferometer locking due to its high and fast electro-optical response [36]. Finally, we expect to further extend this method to advanced light sources such as Kerr combs to generate highly sensitive broadband on-chip gas sensing systems. Hence, our study opens an opportunity to realize compact, sensitive, robust and smart on-chip gas detection for many applications such as smart homes, point-of-care disease diagnostics and wearable devices.

6. Methods

Waveguide fabrication

The LN waveguide is fabricated from a commercially available LN thin film (NANOLN) with a thickness of 500 nm. Designed patterns are first defined in hydrogen silsesquioxane (HSQ) using electron-beam lithography (EBL, 50 keV) and then transferred into the LN layer using optimized argon plasma-based reactive ion etching (RIE). The LN etch depth is 250 nm, leaving a 250-nm-thick slab.

Waveguide modeling

The waveguide model with a rib structure is shown in the inset graph of Fig. 1(b), where $h_1 = h_2 = 250$ nm and $w = 800$ nm. The waveguide sidewall has a 60° trapezoidal shape according to the actual LN nanofabrication process. The electric field of the TE_0 mode at 2004 nm is analyzed by the finite element method. The effective RI (n_{eff}) of the TE_0 mode is calculated to be 1.75. A portion of the evanescent field exists in the air-cladding for gas absorption. The evanescent field factor can be determined by [37]:

$$\Gamma_{air} = n_g \cdot \frac{\iint_{Air} \varepsilon(x,z) \cdot |\boldsymbol{E}|^2 dxdz}{\iint_{-\infty}^{+\infty} \varepsilon(x,z) \cdot |\boldsymbol{E}|^2 dxdz}. \quad (1)$$

where Γ_{air} is the evanescent field factor in the air-cladding, ε is the permittivity of each layer of the LN waveguide, E is the electric field, and n_g is the group index of the TE_0 mode. As a result, the evanescent field factor in the air-cladding is calculated to be 7.4% at the pump wavelength of 2004 nm.

Heat transfer process

We assume that the heat dissipation is invariant along the propagation of the waveguide that allows us to compute the simplified 2D model. Heat conduction is assumed to be the dominant heat transfer process. Since the gas chamber is at a static state, the natural conduction velocity could be much larger than the natural convection velocity. Additionally, the absorption-induced heat relaxation process is fast enough. All of the excited gas molecules at the higher energy state return to the ground state by dissipating energy as heat. Under these assumptions, the 2D photothermal modulation dynamics governed by the heat transfer equation are described as:

$$\rho_g C_g \frac{dT}{dt} + \nabla \cdot (-k_g \nabla T) + \rho_g C_g \boldsymbol{v} \cdot \nabla T = Q \tag{2}$$

$$\rho_s C_s \frac{dT}{dt} + \nabla \cdot (-k_s \nabla T) = 0 \tag{3}$$

$$Q = \sigma \cdot I_{pump\_air}(x, y) \tag{4}$$

where ρ_g and ρ_s are the density of gas and solid, respectively; C_g and C_s are the heat capacity of gas and solid, respectively; k_g, k_s are the heat conductivity of gas and solid, respectively; T is the temperature distribution, v is the gas velocity field, Q is the heat source from the gas heat dissipation, σ is the gas absorption coefficient; and $I_{\text{pump\_air}}$ (x, y) is the pump intensity distribution in the air-cladding, which is determined by the TE_0 mode profile of the waveguide at the pump wavelength.

Heterodyne interferometry

The wavelength modulation of the pump laser generates periodic heating of the waveguide and subsequently leads to the phase modulation of the probe laser propagating in the same waveguide. The phase modulation can be sensitively detected by a heterodyne interferometer. For on-chip PTS, the phase modulation $\Delta\varphi$ is determined by:

$$\Delta\varphi \propto I_{pump} \Gamma_{air} \alpha(v) \tag{5}$$

where I_{pump} is the pump laser intensity, and $\alpha(v)$ is the gas absorbance. As shown in Fig. 6, the beat note is mixed with a 69.8 MHz local oscillator, which is demodulated by the lock-in amplifier (LIA-1) to obtain the phase variation $\Delta\varphi$. Finally, another lock-in amplifier (LIA-2) is used to demodulate the second harmonic photothermal signal (PTS-2*f*). More details of the theory and experimental setup can be found in the literature [38].

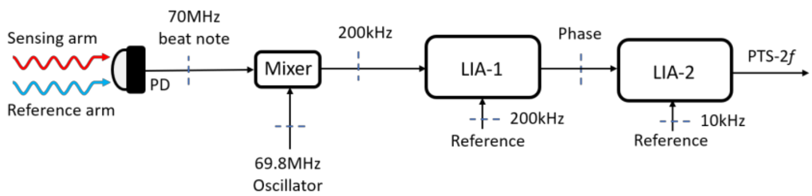

Fig. 6 Schematic of Heterodyne interferometry to extract the photothermal signal PTS-2*f*.

Coupling and propagation loss

To determine the propagation loss, the pump laser is coupled into two LN waveguides with a length of 91.2 mm and 6.5 mm, respectively. According to the difference of the transmitted laser power, we estimate the propagation loss at 2004 nm to be 1.1dB/cm. Note that the ultimate material absorption of LN is less than 0.002 dB/cm [39]. The LN waveguide loss here is mainly caused by the sidewall roughness and the buried SiO_2 material loss 0.12 dB/cm in the substrate [40]. The fiber coupling loss per facet is estimated to be 5.9 dB.

Author contributions

Yue Yan: Conceptualization, Methodology, Validation, Writing – original draft. **Hanke Feng:** Resources, Methodology, Conceptualization, Writing – review & editing. **Cheng Wang:** Resources, Conceptualization, Supervision, Funding acquisition, Project administration, Writing – review & editing. **Wei Ren:** Methodology, Conceptualization, Supervision, Funding acquisition, Project administration, Writing – review & editing.

Conflicts of interest

The authors declare that they have no known competing financial interests or personal relationships that could have appeared to influence the work reported in this paper.

Acknowledgements

This work was supported by Research Grants Council (14209220, 14208221, 11204820), Hong Kong SAR, China; National Natural Science Foundation of China (52122003, 61922092); and Croucher Foundation (9509005).

References

[1] J.W. Wu, G.C. Yue, W.C. Chen, Z.K. Xing, J.Q. Wang, W.R. Wong, et al., On-Chip Optical Gas Sensors Based on Group-IV Materials, ACS Photonics, 7(2020) 2923-40.
[2] A. Farooq, A.B. Alquaity, M. Raza, E.F. Nasir, S. Yao, W. Ren, Laser sensors for energy systems and process industries: Perspectives and directions, Prog. Energy Combust. Sci., 91(2022) 100997.
[3] S. Liu, W. Yan, J. Zhong, T. Zou, M. Zhou, P. Chen, et al., Compact breath monitoring based on helical intermediate-period fiber grating, Sens. Actuators B Chem., 369(2022) 132372.
[4] A. Hänsel, M.J. Heck, Opportunities for photonic integrated circuits in optical gas sensors, J. Phys. Photonics, 2(2020) 012002.
[5] J. Lin, F. Bo, Y. Cheng, J. Xu, Advances in on-chip photonic devices based on lithium niobate on insulator, Photonics Res., 8(2020) 1910-36.
[6] D.S. Su, D.P. Tsai, T.J. Yen, T. Tanaka, Ultrasensitive and selective gas sensor based on a channel plasmonic structure with an enormous hot spot region, ACS Sens., 4(2019) 2900-7.
[7] A. Buzzin, R. Asquini, D. Caputo, G.d. Cesare, Evanescent waveguide lab-on-chip for optical biosensing in food quality control, Photonics Res., 10(2022) 1453.
[8] R. Bi, M.Q. Pi, C.T. Zheng, H. Zhao, L. Liang, F. Song, et al., A niobium pentoxide waveguide sensor for on-chip mid-infrared absorption spectroscopic methane measurement, Sens. Actuators B Chem., 382(2023) 133567.
[9] L. Tombez, E.J. Zhang, J.S. Orcutt, S. Kamlapurkar, W.M.J. Green, Methane absorption spectroscopy on a silicon photonic chip, Optica, 4(2017) 1322-5.
[10] E.J. Zhang, Y. Martin, J.S. Orcutt, C. Xiong, M. Glodde, N. Marchack, et al., Monolithically integrated silicon photonic chip sensor for near-infrared trace-gas spectroscopy, Proc. SPIE., 11010(2019) 110100B.
[11] B. Hinkov, F. Pilat, L. Lux, P.L. Souza, M. David, A. Schwaighofer, et al., A mid-infrared lab-on-a-chip for dynamic reaction monitoring, Nat. Commun., 13(2022) 4753.
[12] M. Vlk, A. Datta, S. Alberti, H.D. Yallew, V. Mittal, G.S. Murugan, et al., Extraordinary evanescent field confinement waveguide sensor for mid-infrared trace gas spectroscopy, Light Sci. Appl., 10(2021) 26.
[13] W.C. Lai, S. Chakravarty, X.L. Wang, C.Y. Lin, R.T. Chen, On-chip methane sensing by near-IR absorption signatures in a photonic crystal slot waveguide, Opt. Lett., 36(2011) 984-6.
[14] M.Q. Pi, C.T. Zheng, H. Zhao, Z.H. Peng, J.M. Lang, J.L. Ji, et al., Mid-infrared ChG-on-MgF_2 waveguide gas sensor based on wavelength modulation spectroscopy, Opt. Lett., 46(2021) 5376-.

[15] F. Ottonello-Briano, C. Errando-Herranz, H. Rodjegard, H. Martin, H. Sohlstrom, K.B. Gylfason, Carbon dioxide absorption spectroscopy with a mid-infrared silicon photonic waveguide, Opt. Lett., 45(2020) 109-12.
[16] C. Ranacher, C. Consani, N. Vollert, A. Tortschanoff, M. Bergmeister, T. Grille, et al., Characterization of Evanescent Field Gas Sensor Structures Based on Silicon Photonics, IEEE Photonics J., 10(2018) 1-14.
[17] C. Ranacher, C. Consani, A. Tortschanoff, R. Jannesari, M. Bergmeister, T. Grille, et al., Mid-infrared absorption gas sensing using a silicon strip waveguide, Sens. Actuator A Phys., 277(2018) 117-23.
[18] E.J. Zhang, L. Tombez, C.C. Teng, G. Wysocki, W.M. Green, Adaptive etalon suppression technique for long-term stability improvement in high index contrast waveguide-based laser absorption spectrometers, Electron. Lett., 55(2019) 851-3.
[19] D. Pinto, J.P. Waclawek, S. Lindner, H. Moser, G. Ricchiuti, B. Lendl, Wavelength modulated diode probe laser for an interferometric cavity-assisted photothermal spectroscopy gas sensor, Sens. Actuators B Chem., 377(2023) 133061.
[20] Y. Qi, F. Yang, Y. Lin, W. Jin, H.L. Ho, Nanowaveguide enhanced photothermal interferometry spectroscopy, J. Light. Technol., 35(2017) 5267-75.
[21] J.P. Waclawek, C. Kristament, H. Moser, B. Lendl, Balanced-detection interferometric cavity-assisted photothermal spectroscopy, Opt. Express, 27(2019) 12183-95.
[22] W. Jin, Y. Cao, F. Yang, H.L. Ho, Ultra-sensitive all-fibre photothermal spectroscopy with large dynamic range, Nat. Commun., 6(2015) 6767.
[23] M. Hu, A. Ventura, J.G. Hayashi, F. Poletti, S. Yao, W. Ren, Trace gas detection in a hollow-core antiresonant fiber with heterodyne phase-sensitive dispersion spectroscopy, Sens. Actuators B Chem., 363(2022) 131774.
[24] Q. Wang, Z. Wang, H. Zhang, S. Jiang, Y. Wang, W. Jin, et al., Dual-comb photothermal spectroscopy, Nat. Commun., 13(2022) 2181.
[25] D. Zhu, L. Shao, M. Yu, R. Cheng, B. Desiatov, C. Xin, et al., Integrated photonics on thin-film lithium niobate, Adv. Opt. Photonics, 13(2021) 242-352.
[26] A. Boes, L. Chang, C. Langrock, M. Yu, M. Zhang, Q. Lin, et al., Lithium niobate photonics: Unlocking the electromagnetic spectrum, Science, 379(2023) eabj4396.
[27] M. Seiter, D. Keller, M.W. Sigrist, Broadly tunable difference-frequency spectrometer for trace gas detection with noncollinear critical phase-matching in LiNbO3, Appl. Phys. B, 67(1998) 351-6.
[28] J.Y. Zhang, Y.M. Sua, J.Y. Chen, J. Ramanathan, C. Tang, Z. Li, et al., Carbon-dioxide absorption spectroscopy with solar photon counting and integrated lithium niobate micro-ring resonator, Appl. Phys. Lett., 118(2021) 171103.
[29] D. Pohl, M.R. Escale, M. Madi, F. Kaufmann, P. Brotzer, A. Sergeyev, et al., An integrated broadband spectrometer on thin-film lithium niobate, Nat. Photonics, 14(2020) 24-9.
[30] C. Wang, M. Zhang, M.J. Yu, R.R. Zhu, H. Hu, M. Loncar, Monolithic lithium niobate photonic circuits for Kerr frequency comb generation and modulation, Nat. Commun., 10(2019) 978.
[31] M. Zhang, B. Buscaino, C. Wang, A. Shams-Ansari, C. Reimer, R.R. Zhu, et al., Broadband electro-optic frequency comb generation in a lithium niobate microring resonator, Nature, 568(2019) 373–7.
[32] P.E. Ciddor, Refractive index of air: new equations for the visible and near infrared, Appl. Opt., 35(1996) 1566-73.
[33] L. Moretti, M. Lodice, F.G.D. Corte, I. Rendina, Temperature dependence of the thermo-optic coefficient of lithium niobate, from 300 to 515 K in the visible and infrared regions, J. Appl. Phys., 98(2005) 253-76.
[34] Y. Fu, T. Ye, W. Tang, T. Chu, Efficient adiabatic silicon-on-insulator waveguide taper, Photonics Res., 2(2014) A41-A4.
[35] A. Vasiliev, A. Malik, M. Muneeb, B. Kuyken, R. Baets, G.n. Roelkens, On-chip mid-infrared photothermal spectroscopy using suspended silicon-on-insulator microring resonators, ACS Sens., 1(2016) 1301-7.

[36] G. Martin, S. Heidmann, J.-Y. Rauch, L. Jocou, N. Courjal, Electro-optic fringe locking and photometric tuning using a two-stage Mach–Zehnder lithium niobate waveguide for high-contrast mid-infrared interferometry, Opt. Eng., 53(2014) 034101.
[37] J.T. Robinson, K. Preston, O. Painter, M. Lipson, First-principle derivation of gain in high-index-contrast waveguides, Opt. Express, 16(2008) 16659-69.
[38] C. Yao, S. Gao, Y. Wang, W. Jin, W. Ren, Heterodyne interferometric photothermal spectroscopy for gas detection in a hollow-core fiber, Sens. Actuators B Chem., 346(2021) 130528.
[39] V.S. Ilchenko, A.A. Savchenkov, A.B. Matsko, L. Maleki, Nonlinear optics and crystalline whispering gallery mode cavities, Phys. Rev. Lett., 92(2004) 043903.
[40] M.A. Khashan, A.Y. Nassif, Dispersion of the optical constants of quartz and polymethyl methacrylate glasses in a wide spectral range: 0.2-3 um, Opt. Commun., 188(2001) 129-39.

Author biographies:

Yue Yan received his B.S. and M.S. degree from NanChang University and Tianjin University. He is currently working toward the Ph.D. degree with the Department of Mechanical and Automation Engineering, The Chinese University of Hong Kong, Hong Kong. His research interests include optical sensing and laser spectroscopy.

Hanke Feng received his B.S. and M.S. degree from Xi'an University of Technology and Xi'an Jiaotong University. He is currently working toward the Ph.D. degree with the Department of Electrical Engineering, City University of Hong Kong, Hong Kong. His research interest focuses on design and nanofabrication technology of integrated lithium niobate photonic circuits.

Cheng Wang received his B.S. degree in Microelectronics from Tsinghua University, Beijing, China, in 2012 and the Ph.D. degree in Electrical Engineering from Harvard University, in 2017. From 2017 – 2018, Cheng conducted research as a postdoctoral fellow at Harvard, before joining City University of Hong Kong as an Assistant Professor in June 2018. Dr. Wang's research focuses on the design and nanofabrication technology of integrated photonic devices and circuits. His current research effort focuses on realizing integrated lithium niobate photonic circuits for applications in optical communications, millimeter-wave/terahertz technologies, nonlinear optics, and quantum photonics.

Wei Ren received the B.S. degree in mechanical engineering and automation from Tsinghua University, Beijing, China, in 2006, and the Ph.D. degree in mechanical engineering from Stanford University, Stanford, CA, USA, in 2013. He is currently an Associate Professor with the Department of Mechanical and Automation Engineering, The Chinese University of Hong Kong, Hong Kong. After the graduation degree, he was a Postdoctoral Fellow with the Department of Electrical and Computer Engineering, Rice University, Houston, TX, USA. His research interests include laser spectroscopy, optical sensing, and combustion and propulsion. He is a Senior Member of Optica.

Declaration of interest statement:

The authors declare that they have no known competing financial interests or personal relationships that could have appeared to influence the work reported in this paper.